Electrochimica Acta 549 (2026) 148035

Contents lists available at ScienceDirect

Electrochimica Acta

journal homepage: www.journals.elsevier.com/electrochimica-acta

High-performance low-power Photoelectrochemical photodetector functionalized by titanium Diselenide thin film

Kevin Kantilal Bhanderi [a,*], Preet Deepankumar Vyas [a], Jay Bhadreshbhai Ka. Patel [a], Devang Dhorada [a], Akshaybhai J. Patel [b], Vismay Trivedi [c], Shubham Umeshkumar Gupta [b,d], Franco Mayanglambam [e], Arun Anand [a], Kireetkumar D. Patel [a,b,*]

[a] Department of Physics, Sardar Patel University, Vallabh Vidyanagar, 388120, Gujarat India
[b] Semiconductor Science and Technology Programme, Department of Physics, Sardar Patel University, Vallabh Vidyanagar, 388120, Gujarat India
[c] Department of Aerospace Structures and Materials, Delft University of Technology, Kluyverweg 1, 2629 HS, Delft, The Netherlands
[d] Photoelectric and Energy Device Application Lab (PEDAL), Department of Electrical Engineering, Incheon National University, Incheon, 22012, Republic of Korea
[e] Centre for Nanotechnology, IIT Guwahati, Assam 781039, India

ARTICLE INFO

Keywords:
Titanium diselenide ($TiSe_2$)
2D TMDC photodetector
Photoelectrochemical photodetector
Optoelectronic sensor

ABSTRACT

Titanium Diselenide ($TiSe_2$) thin films have become attractive options for high-performance optoelectronic devices due to their exceptional optical and electronic properties and distinctive layered structure. However, despite their promise, $TiSe_2$ has not been well explored for Photoelectrochemical photodetector applications, especially when it comes to improving its carrier dynamics, stability, and spectrum response under operating circumstances. Present article demonstrates significant advancement in the field by utilization of large area $TiSe_2$ thin film for fabrication of high-performance photoelectrochemical photodetector (PEC-PD). Herein, $TiSe_2$ crystalline powder is grown using direct vapour transport technique followed by elemental and morphological confirmation via Energy Dispersive X-ray Analysis and Field Emission Scanning Electron Microscopy that revealed layered hexagonal structure along with maintaining stoichiometry. From the grown compound of $TiSe_2$, thin films are deposited by physical vapour deposition and well characterised. Powder X-Ray Diffraction analysis confirmed hexagonal structures whereas Raman spectroscopy identified the vibrational modes of $TiSe_2$ in thin film. Atomic Force Microscopy portrayed surface smoothness along with uniformity. This large area $TiSe_2$ thin film is utilised as working electrode in the application of PEC-PD that demonstrated optimum performance by achieving high detectivity of about $7.36 \pm 0.02 \times 10^8$ Jones under low-power operation of 100 mV bias. The device indicated rapid photoresponse dynamics by exhibiting a rise and decay time of 12 ms and 33 ms respectively. To the best of our knowledge, this is the first report of a $TiSe_2$ thin-film-based PEC-PD. Outcome of current study showcases the potential of $TiSe_2$ in facilitating fabrication of high-performance optoelectronic devices.

1. Introduction

Optoelectronic devices like photodetector and phototransistor play a vital role in development of advanced society, with versatile applications in areas such as optical communication, environmental monitoring, national defence, providing operation in extreme conditions [1–4]. As photodetection technology advances, there is an increasing interest in developing detectors that are more sensitive, selective, and capable of operating across a broad range of wavelengths [5–7]. However, these photodetectors sometimes face challenges in terms of sensitivity and long-term stability. Photoelectrochemical photodetectors (PEC-PDs) are emerging as a promising alternative, leveraging both optical absorption and electrochemical reactions to achieve enhanced photodetection [2,8–11]. PEC-PD typically consist of a semiconducting material immersed in an electrolyte, where the incident light generates photocurrents due to light-induced charge separation and redox reactions. This approach offers advantages such as improved sensitivity due to the electrochemical reaction induced enhancement of signals and greater stability, which is particularly beneficial for light harvesting applications [8,12,13].

* Corresponding authors.
E-mail addresses: kkbhanderi206@gmail.com (K.K. Bhanderi), kdpatel-phy@spuvvn.edu (K.D. Patel).

https://doi.org/10.1016/j.electacta.2025.148035
Received 12 August 2025; Received in revised form 16 December 2025; Accepted 17 December 2025
Available online 18 December 2025

Transition metal dichalcogenides (TMDCs) with chemical formula MX_2 (where M is transition metal atom and X is chalcogen atom) are among two dimensional (2D) materials. These layered materials have gained lots of attention due to their profound device applications as field-effect transistors, chemical sensors, optoelectronic devices, piezoelectric nano energy generators, electrochemical energy storage, and catalytic energy conversion [14–18]. Furthermore, it is well known that various kinds of TMDCs such as MoS_2, WS_2, $MoSe_2$, WSe_2, and TiS_2 have been synthesized that were at the forefront of optoelectronic research and being explored for applications in wearable devices, biomedical sensors, field-effect transistors (FETs), phototransistors, and photovoltaics [19–28]. To name a few, Vashistha et al. have shown monolayer MoS_2 and GaN thin film heterostructure for a self-powered and bidirectional photodetector which attains a peak responsivity 631 mAW^{-1} at zero bias [29], Shin et al. have worked on large-area 2D flexible WS_2/MoS_2 heterojunction interface using a hexagonal boron nitride (h-BN) interlayer shows enhanced detectivity, responsivity and EQE [30]. Together with these materials, $TaSe_2$ and TaS_2, which are semiconducting materials and belong to the nearby group IVB, have recently shown exceptionally high responsivity and ultra-broadband response [31,32]. Payal et al. reported the flexible self-powered PEC-PD based on $TaSe_2$ nanocrystals that achieved the highest photocurrent density of 20.8 $\mu A/cm^2$ and photoresponsivity of 0.208 mA/W in 0.5 M KOH solution [33]. All these basic investigations have potential for advancing our understanding of the optoelectronic characteristics of group IVB materials [32,34–37].

Among, the IVB materials, titanium diselenide ($TiSe_2$) has recently garnered significant attention due to its unique properties. $TiSe_2$ has a narrow bandgap and with high in-plane excellent charge transport properties enable faster transport of photogenerated carriers and reduces internal resistance of device under test. The material also exhibits charge-density-wave related modulation in its density of states, which enhances light matter interaction and broadens its usable spectral response [38–42]. Changying Xiong et al. reported that 2D $TiSe_2$ enables fast and uniform memristive switching with fairly low threshold voltages and high cycle-to-cycle consistency [43]. Thayer S. Walmsley et al. demonstrated an enhancement in photocurrent speed using $TiSe_2$ with metal junctions [39]. These attributes of $TiSe_2$ make it an ideal candidate for photodetection. Importantly, $TiSe_2$ small indirect bandgap promotes efficient charge transfer across the semiconductor-electrolyte interface, lowering interfacial barriers for carrier injection compared with many other TMDCs. These combined properties such as fast interface kinetics, high conductivity and strong optical coupling make $TiSe_2$ particularly suitable for PEC-PD, offering functional behaviour that is not easily achieved with standard TMDC materials. Although $TiSe_2$ has been extensively characterized regarding its fundamental charge density wave (CDW) physics [44] and general optoelectronic properties [45], the implementation of large-area, thermally evaporated $TiSe_2$ thin films as photoelectrochemical photodetectors (PEC-PDs) has not been previously reported. Existing literature has predominantly focused on exfoliated flakes [46], theoretical modelling [41], or $TiSe_2$ based heterostructures for storage applications [47]. To the best of our knowledge, this work presents the first demonstration of a PVD-deposited $TiSe_2$ working electrode achieving competitive PEC-PD performance metrics, specifically a detectivity of $7.36 \pm 0.020 \times 10^8$ Jones (at 100 mV bias) and rise/decay times of 12 ms and 33 ms, respectively. Such advancements make $TiSe_2$ based PEC-PD a highly adaptable, potentially serving as key components in future multifunctional photodetection systems.

2. Experimental methodology

2.1. $TiSe_2$ synthesis and thin film formation

High purity crystals along with crystalline compound of $TiSe_2$ were grown using Ti powder having (98.50 %) and Se powder having (99.99 %) purity procured from Hi-media and SRL respectively. For the growth of crystals and compounds, a chemically cleaned quartz ampoule underwent hydrofluoric acid treatment along with heating treatment which is necessity for the etching of inner wall of ampoule to establish nucleation centres. Herein, HF is handled with great care as reported in material safety data sheet (MSDS)[48] due to its flammable and toxic nature. To eliminate any water or organic residue and ensure contamination-free walls, the ampoule was dried at 383 K for 24 h in the hot-air-oven. Following stoichiometric proportions, pure titanium (Ti) and selenium (Se) powders were added inside the cleaned ampoule, which was then sealed under high vacuum ($\approx 10^{-5}$ mbar) and placed horizontally in a PID-controlled dual zone high-temperature furnace as illustrated in Fig. 1.

The furnace comprises a source zone and a growth zone, with source materials positioned in the former and nucleation sites on the inner surface in the latter. The crystal growth utilized the Direct Vapor Transport (DVT) method, incorporating a four-step temperature profile: initial heating to 1223 K and 1183 K for the source and growth zones, respectively; a constant temperature phase maintained for 80 h to facilitate the reaction of source materials in the vapor phase. At this stage, 40 K temperature gradient between the two zones, creates a vapor pressure gradient that helps the mass transport of reacted compound from the source zone to the growth zone. In the third stage, cooling to 923 K and 883 K at rates of approximately 6 K/hour; and finally, cooling to room temperature at rates of about 46 K/hour and 44 K/hour for the source and growth zones, respectively.

Highly crystalline ingots of $TiSe_2$ were collected from ampoule and it was grinded by agate mortar pestle for making fine powder. This powder is used for the thin film deposition. Hind High Vacuum (HHV) makes thermal evaporation unit is used to deposit the thin film of $TiSe_2$ compound having 500 nm thickness with the high vacuum of about 10^{-6} mbar at the deposition rate of 2Å/s. The thickness and deposition rate of deposited thin film were maintained by SQC 310A digital thickness monitor. These thin films were then used for further characterization and preparation of PEC-PD.

2.2. Characterization techniques and tools

Surface morphology and elemental confirmation of synthesised materials were done using Field Emission Scanning Electron Microscopy (FESEM) and Energy Dispersive X-ray (EDX) Analysis techniques respectively. After verification of grown compound, thin films of $TiSe_2$ were deposited and characterized. Thin film's structural confirmation was done by powder X-Ray diffractometer (Bruker PXRD) with Cu-K_α radiation source having a wavelength of 1.5418 Å. Atomic vibrational modes are observed by Raman spectroscopy (RENISHAW In-via Raman microscope with 532 nm excitation laser). Atomic Force Microscopy AFM (HORIBA) was used to observe surface topography with scanning area of 9 μm^2.

2.3. Photoelectrochemical photodetector characteristics measurement setup

The experimental setup to characterize the photoresponse of the fabricated PEC-PD based on $TiSe_2$ thin films, along with the reaction mechanism, is depicted in Fig. 2. In this setup, 0.5 M Na_2SO_4 was used as the electrolyte. A $TiSe_2$ thin film deposited on an ITO substrate served as the photoanode, while a copper wire acted as the cathode. A 405 nm wavelength laser diode with an optical power of 200 mW was used to illuminate the PEC-PD. The light intensity is modulated by a mechanical chopper controlled by an Arduino microcontroller. In this setup, the PEC-PD sample is placed on a linear translation stage, which allows for precise variation of the sample's axial position relative to the laser beam. The laser is passed through a microscope objective lens, which causes the laser beam to expand before it strikes the sample's effective area (0.64 cm^2). By adjusting the axial position of the sample using the

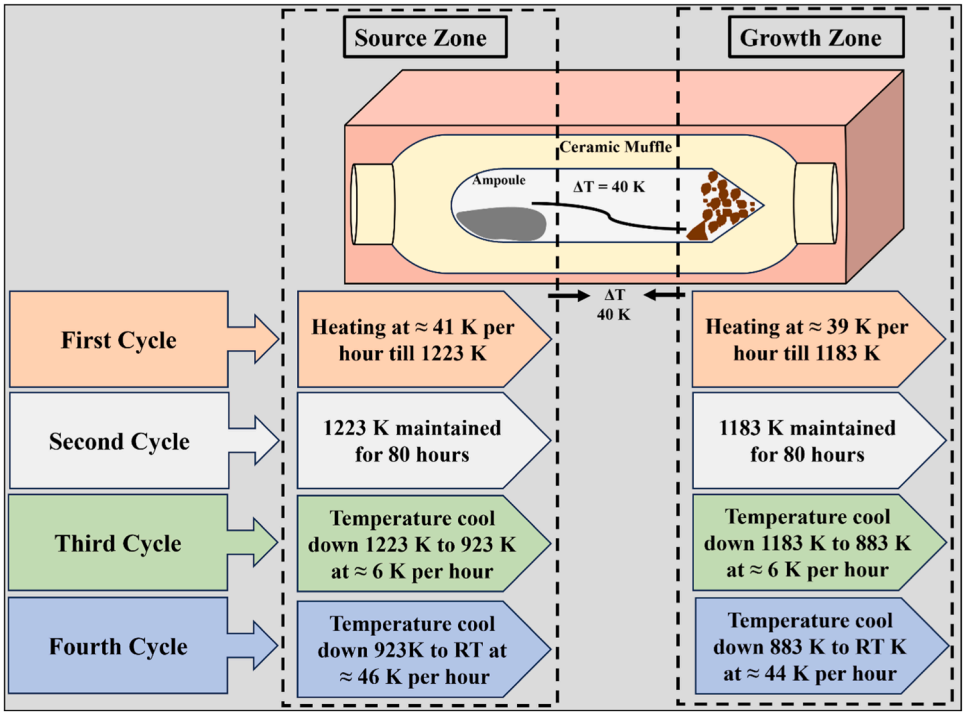

Fig. 1. Schematic diagram of PID controlled high temperature dual zone furnace with temperature profile.

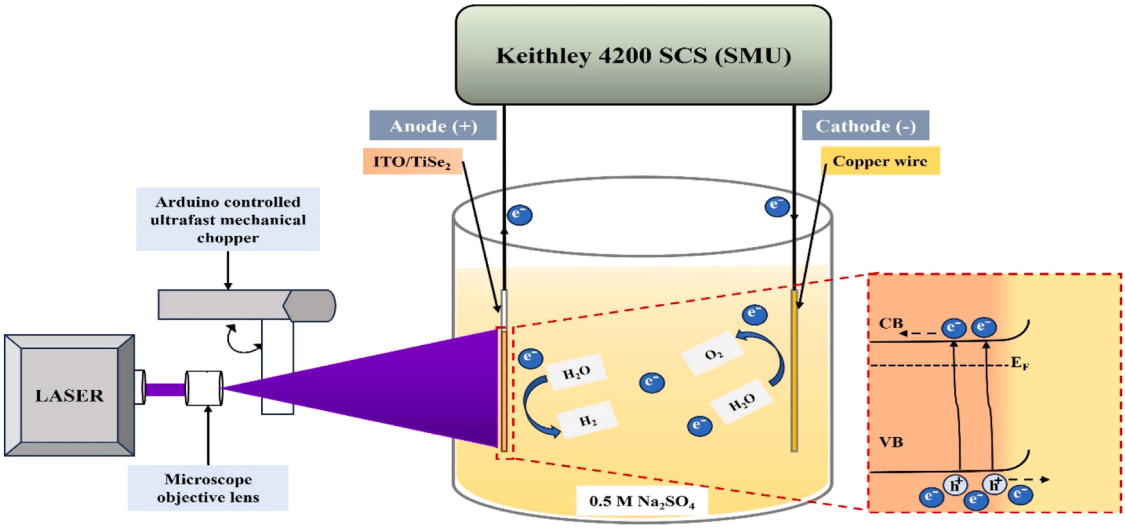

Fig. 2. Experimental setup of photoresponse of PEC PD based on $TiSe_2$ thin film, with reaction mechanism.

translation stage, the incident light power density on the sample can be precisely controlled in the range of 8.47–105.93 mW/cm^2, enabling systematic variation of the optical power falling on the detector. A laser power meter (Thorlabs PM-400) is used to measure and calibrate the system at various axial positions, ensuring that the optical power density at these specific positions is known. This calibration allows for accurate control over the power incident on the sample, providing reliable power values at each stage position. The photodetection properties of the PEC-PD based on $TiSe_2$ thin films are then characterized at 100 mV to 500 mV applied bias, using the Keithley 4200 Semiconductor Characterization System (SCS), which enables detailed analysis of the sample's photoresponse. The Optical images of Experimental setup is shown in figure S (1) and S(2).

3. Results and discussion

Highly pure crystals and crystalline powder of $TiSe_2$ (Titanium diselenide) were grown using DVT technique by PID controlled high temperature dual zone furnace. Grown $TiSe_2$ crystalline powder was inspected by EDX spectra analysis, in which elemental peaks of Ti and Se are observed as shown in Fig. 3(a) and FESEM was used to study surface morphology of $TiSe_2$ as shown in Fig. 3(b and c). The FESEM images revealed distinct morphological features at different magnifications. Fig. 3(b), upon closer examination, reveals the layered growth of the material, while Fig. 3(c) clearly shows a well-defined hexagonal structure. Fig. 3(d–f) presents the elemental mapping results, confirming the homogeneous distribution of each element across the entire scanned region. Specifically, Fig. 3(d) and Fig. 3(e) display the elemental mappings for Ti and Se, respectively, while Fig. 3(f) illustrates the combined

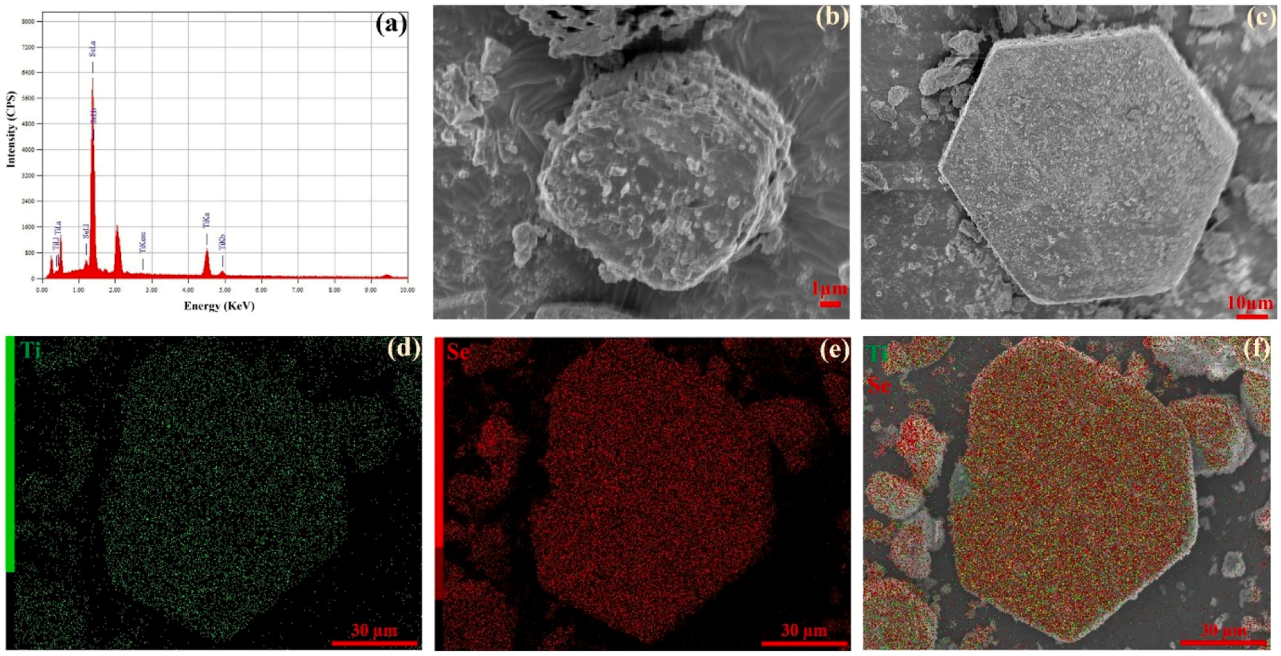

Fig. 3. Surface morphology and elemental confirmation: (a) EDX spectra, (b-c) FESEM images of $TiSe_2$ crystalline powder, (d-f) Elemental mapping.

mapping of both detected elements.

After elemental confirmation of grown compound of $TiSe_2$. The powder was used to deposit the thin films. Large area thin films of $TiSe_2$ were deposited by PVD method using thermal evaporation technique. The XRD spectra of $TiSe_2$ thin film provided critical insights of the crystallographic structure and phase composition. The hexagonal lattice structure of deposited thin film was confirmed by XRD spectra with Cu-Kα radiation imparted on the thin film sample scanned at 2θ angles between 5–80° as shown in Fig. 4(a). The strong diffraction peaks observed at 2θ angles 29.72, 41.32, 45.4 and 51.7 are corresponding to (002), (012), (003) and (110) crystalline planes respectively. The sharpness and well-defined nature of these peaks confirm the high crystallinity of the thin film. Additionally, quantitative analysis of XRD pattern leads to determination of several structural parameters. Herein, the crystallite size calculated to be approximately 24.71 nm using Debye Scherrer equation with Scherrer constant (K) value 0.94. Moreover, micro strain and dislocation density are estimated to be 5.72×10^{-3} and 1.63×10^{15} lines m^{-2} respectively. Peaks marked with asterisks (*) belong to the underlying substrate. XRD pattern do not show any extra impurity peaks and has good agreement with standard ICDD

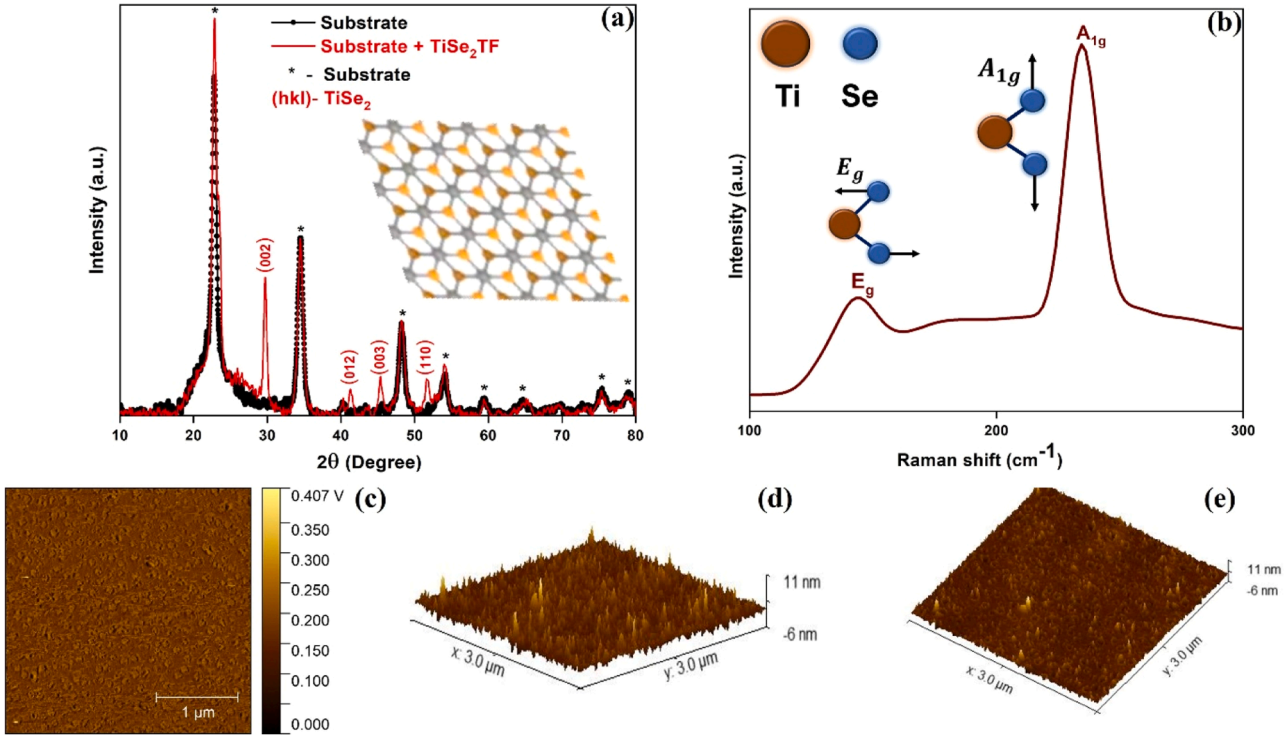

Fig. 4. Structural, vibrational and topography of $TiSe_2$ thin film: (a) XRD spectra, (b) Raman Spectra, (c - e) AFM Images.

#01–083–0980 as well as previously reported structural information of $TiSe_2$[17,47,49]. The inset schematic representation shown in Fig. 4(a) represents the hexagonal lattice structure of $TiSe_2$ where each titanium (Ti) atom is sandwiched between two layers of selenium (Se) atoms, forming a layered van der Waals crystal. In this 1T-phase of $TiSe_2$ structure, the Ti atoms are octahedrally coordinated with Se atoms and forming a trigonal prismatic geometry within the plane. Herein, the unit cell belongs to the space group $P\bar{3}m1$ which is a characteristic of hexagonal symmetry [44]. The Raman spectrum further confirms the vibrational modes characteristic of $TiSe_2$ thin films as shown in Fig. 4(b). Two Raman peaks are observed at 144.63 cm^{-1} and 234.39 cm^{-1} corresponding to E_g and A_{1g} vibrational modes, respectively [50,51]. The inset diagram shows the vibrational directions of Ti and Se atoms corresponding to E_g (in plane) and A_{1g} (out of plane) vibrational modes. Previous studies on bulk $TiSe_2$ crystals report Raman active modes at 144 cm^{-1} (E_g) and 205 cm^{-1} (A_{1g})[44]. In the present work these modes exhibit noticeable shifts, particularly a pronounced upshift of the A_{1g} mode in the thermally evaporated $TiSe_2$ thin film. Such deviations from bulk Raman frequencies are commonly observed in thin films due to residual strain introduced during deposition, which alters interlayer coupling and phonon confinement effects compared to bulk crystals. The observed upshift corresponds to an effective out of plane compressive strain of 5.6 %[52,53]. These results demonstrate that residual strain plays key role in modifying phonon frequencies and lattice dynamics in thin film $TiSe_2$. The sharpness and intensity of these modes validate the good stoichiometry of the $TiSe_2$ thin film [44,51].

The AFM scans were captured over an area of 9 μm^2 to investigate the surface morphology, uniformity and roughness characteristics of the $TiSe_2$ thin film which is providing nanoscale resolution of the topographic features as shown in Fig. 4(c–e). Fig. 4(c) shows a 2D height map of the surface that is revealing a homogeneous distribution of granular structures across the scanned area. The uniform contrast indicates a relatively smooth surface with low variation in height. This suggests a consistent grain size and minimal agglomeration which is ensuring uniformity along with good quality of thin film. Fig. 4(d and e) provides a 3D topographical view of the same scan area. The height variation ranges from approximately −6 nm to +11 nm, indicating a moderately smooth surface morphology with nanoscale features. These surface ripples are typically associated with the nucleation and growth dynamics of layered van der Waals materials. The fine-grained texture and absence of large clusters or cracks confirm high-quality of thin film. The film displays dense, uniformly distributed grains with no prominent pits or voids which is confirming the continuity of the film and the absence of pinholes or delamination issues. Herein, surface appears very smooth with minimal irregularities having RMS roughness of surface is about 1.76 nm which is falling in acceptable range for device-quality thin films. Such smooth and defect-free morphology is critical for ensuring good electrical contact, stable carrier transport and consistent optical response. Herein, this level of surface uniformity helps minimize trap-assisted recombination and carrier scattering at nanoscale surface features [54]. This promotes more efficient charge transfer at the semiconductor electrolyte interface during PEC operation. The reliable and stable photocurrent behaviour further confirms that surface morphology is not a major factor contributing to recombination losses in this film. The observed surface quality correlates well with the XRD and Raman results, reinforcing the structural integrity and crystallinity of the $TiSe_2$ film.

The schematic shown in Fig. 2 depicts charge separation and conduction mechanism involved when $TiSe_2$ is used as photoanode. When an N-type material ($TiSe_2$ in present study) comes in contact with an electrolyte, electrons diffuse from semiconductor to the solution until the fermi level alignment is achieved, generating a space-charge region within the semiconductor. This establishes a built-in electric field, directed from semiconductor to electrolyte, which facilitates separation of photogenerated electron–hole pairs by driving holes toward the electrolyte interface and electrons into the bulk semiconductor. Upon illumination of the photoelectrochemical photodetector (PEC-PD), photogenerated holes in $TiSe_2$ migrate to the semiconductor–electrolyte interface, where they participate in oxidation reactions described by: $4h^+ + 2H_2O(l) \rightarrow O_2(g) + 4H^+$. Simultaneously, electrons collected by the conductive ITO back contact are transported externally toward the copper counter electrode for the photoreduction of water: $2e^- + 2H_2O(l) \rightarrow H_2(g) + 2OH^-$[10,55]. This coupled redox reaction complete the electrical circuit through the Na_2SO_4 electrolyte, enabling charge flow and a low-powered photoresponse. Under the present conditions, 0.5 M Na_2SO_4 was used as an electrolyte because of its key role in sustaining a stable and high performing photoelectrochemical operation. Na_2SO_4 serves as an inert supporting electrolyte wherein it provides high and stable ionic environment for efficient charge transport through the electrolyte, without getting involved in any redox reaction at the semiconductor interface. High ionic strength of Na_2SO_4 compresses the electric double layer at the semiconductor-electrolyte interface leading to increase in Helmholtz capacitance and stabilization of the interfacial potential, which helps sustain the built-in electric field generated by band bending in $TiSe_2$[56,57]. Moreover, chemical inertness of Na_2SO_4 avoids unwanted surface reactions or degradation of the $TiSe_2$ photoanode, ensuring reproducible and stable device performance under illumination. Applying a small forward bias (100 mV in present study) improves the built-in electric field, effectively increasing the potential difference driving charge carrier separation and transport. This bias reduces recombination by enhancing carrier drift velocities, minimizing carrier transit times across the depletion region, and increasing the probability of photogenerated carriers reaching their respective electrodes before recombining.

The detector parameters of PEC-PD, such as photocurrent (I_{PC}), Photocurrent density (I_{PCD}), Responsivity (R_{Ph}) and Detectivity (D) are evaluated using following Eqs. (1–4)[58,59].

$$I_{PC} = I_{LC} - I_{DC} \tag{1}$$

Where, I_{LC} refers to the current of PEC PD when the light is switched ON, while I_{DC} refers to the current of PEC PD when the light is switched OFF.

$$I_{PCD} = \frac{I_{PC}}{S} \tag{2}$$

$$R_{PH} = \frac{I_{PC}}{P * S} \tag{3}$$

$$D = R_{PH} * \sqrt{\frac{S}{2\ q\ I_{DC}}} \tag{4}$$

Where, S represents the device effective area (0.64 cm^2) of $TiSe_2$ thin film and q is charge of electron. The Rise time and decay time are also very important parameters that reveal switching behaviour of any photodetector.

The performance assessment of the PEC-PD begins with its spectral responsivity, offering clarity on the wavelength that provides maximum output. To evaluate the spectral responsivity, laser sources of wavelengths 405 nm, 532 nm, 635 nm, 780 nm, and 850 nm were employed, with all wavelength calibrated to an identical power density of 1.41 mW/cm^2. The device exhibits a response over a broad range of wavelengths. The resulting spectral response is presented in Fig. 5(a). Subsequent device performance was assessed using 405 nm light with various incident power densities and applied bias voltages.

The photo response curves, depicting photocurrent verses time of the PEC-PD were obtained using 405 nm wavelength monochromatic light source with 10 s periodic exposure to the detector. The resultant photocurrent was measured by Keithley 4200 SCS. The measurements were conducted with illumination of different light power densities ranging from 8.47 – 105.93 mW/cm^2, with an external bias of 100 mV. When light suddenly illuminates the ITO/$TiSe_2$ interface, current

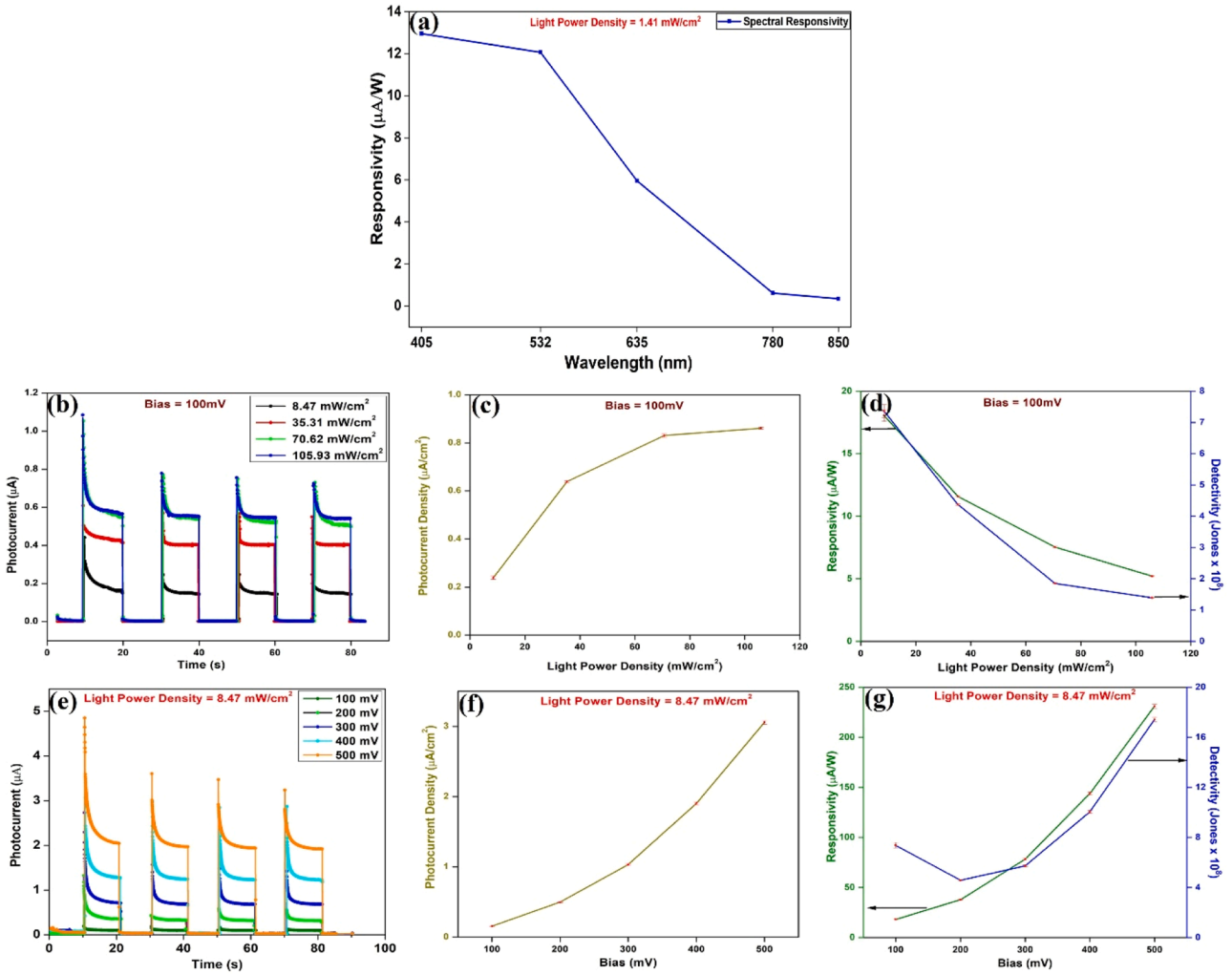

Fig. 5. Pulse-photoresponse of $TiSe_2$ thin film PEC-PD: (a) Spectral Responsivity at 1.41 mW/cm^2 (b) Light power densities (8.47–105.93 mW/cm^2) dependent pulse photoresponse at 100 mV bias, (c) Photocurrent density Vs light Power density variation, (d) Responsivity and Detectivity Vs light power density Variation Photocurrent density Vs light Power density variation, (e) Bias dependent pulse photoresponse at 8.47 mW/cm^2 light power density (f) Photocurrent density Vs bias variation, (g) Responsivity and Detectivity at bias (100–500) mV.

overshoot and transient spikes are observed as shown in Fig. 5(b) and Fig. 5(e), followed by reduction observed in current spikes due to the charging and discharging effect of trap states. Herein, over the repeated pulses a growing number of deep traps gradually filled and do not release charge quickly, so limited number of free carriers available for subsequent spikes [1,60]. This trap saturation combined along with slow ion movement at the interface, which cause gradually shifts in the surface potential over time, leading to progressive reduction in a spike height [55]. With increasing incident light power density, higher numbers of photo-carriers are generated leading to increase in photocurrent as shown in Fig. 5(b). Besides this, photocurrent relation with light power density reveals a distinct sub-linear dependence on the incident light power density, indicating that the device does not respond proportionally to increasing illumination intensity. This sub-linearity arises mainly from the saturation of shallow trap states and the enhanced probability of trap-assisted recombination at higher light power densities. This behaviour is well described by the empirical power-law relation $"I_{ph} \propto P^{\gamma}"$, where $'\gamma'$ represents the weaker-trapping coefficient [61]. Our measured photocurrent resulted a $'\gamma'$ value of 0.54 indicating the presence of band-edge trap states that play a crucial role in the material's recombination processes.

Accordingly, the variation in photocurrent density with incident light power density is presented in Fig. 5(c). Fig. 5(d) demonstrates dependence of responsivity and detectivity on incident illumination light power density. The higher light power density of incident light results in higher recombination rates due to large number of photo carriers now available for the recombination [62]. Additionally, this excessive carrier population tends to accumulate near the interface under strong illumination and builds up space charge layer. The presence of this space charge reduces the strength of the built-in electric field that normally drives the separation and transport of photo-generated carriers [63]. As the internal field becomes screened and slightly flattened due to this accumulation, the drift-assisted carrier collection becomes less efficient. Each additional photon contributes less effectively to the useful photocurrent, leading to reduced responsivity at higher light power density [64]. At constant applied bias, detectivity becomes directly proportional to responsivity and follows the same power-dependent trend as responsivity. To evaluate bias-dependent behaviour, transient photocurrent measurements were repeated at biases from 100 to 500 mV under periodic illumination having power density of about 8.47 mW/cm^2, as shown in Fig. 5(e). A monotonic increase of photo current density with bias is observed Fig. 5(f), rising from 0.15 μA cm^{-2} at 100 mV to 3.05 μA cm^{-2} at 500 mV. This enhancement is attributed to the increased electric field, which acts in agreement with internal electric field and improves charge-carrier drift velocity and reduces carrier recombination losses within the active

region. The responsivity curve in Fig. 5(g) shows increase with bias, reaching 230.95 ± 2.14 μA W^{-1} at 500 mV. Higher bias generates a stronger field that more effectively sweeps photogenerated electrons and holes toward their respective electrodes before recombination, thereby increasing the ratio of collected charge to incident photon flux. Unlike responsivity, detectivity depends on both dark current and photocurrent. Initially, as bias increases to 200 mV, the dark current rises more rapidly than responsivity, causing a slight dip in detectivity. Beyond this threshold, the responsivity enhancement outpaces the dark-current increase, resulting in a pronounced increase in detectivity up to 1.74 ± 0.02 × 10^9 Jones at 500 mV. This nonmonotonic trend reflects that increased responsivity. Furthermore, the key figures of merit such as Noice Equivalent Power (NEP) and External Quantum Efficiency (EQE) were determined using standard photodetector equations to provide a reliable performance benchmark [64,61]. The NEP is found to be 1.09 × 10^{-9} W $Hz^{-1/2}$, whereas the EQE is found to be 0.0055 %. These results establish a reference performance for this material system and highlight opportunities for further improvement through optimized interfaces and enhanced light management.

Fig. 6(a) shows the temporal variation of photocurrent when the device is subjected to periodic light illumination. Herein, the rise time (τ_{rise}) characterizes the speed at which photogenerated carriers are generated and separated under illumination whereas the decay time (τ_{decay}) characterizes the recombination and relaxation dynamics of photogenerated carriers following termination of illumination. As shown in insets of Fig. 6(a), τ_{rise} of fabricated PEC-PD is defined as the time it takes for the photocurrent to increase from 10 % to 90 % of its steady state photocurrent value. Similarly, τ_{decay} is defined as the time it takes for the photocurrent to decrease from 90 % to 10 % of its steady state photocurrent value [65,66]. The inset plots provide a closer look at the rise time of about 12 ms and decay time of about 33 ms. This detailed view complements the plateau seen after the initial rise in Fig. 6(a), reflects a quasi-steady regime, where trap states become filled and the rates of carrier extraction and recombination temporarily match. As demonstrated in previous reports that, balance results in a short, nearly constant photocurrent response before the final steady-state value is reached [67]. The sharp transitions and minimal time constants suggest that the $TiSe_2$ thin film has fast response kinetics, making it suitable for real-time light detection and switching applications. The stability of the PEC-PD was evaluated under continuous periodic light exposure via repeated light on/off for 20 cycles, which is one of the main factors to assess performance parameters and suitability for long term application of detector. Fig. 6(b), illustrates the device pulse photo response over 400 s of continuous periodic illumination. Photo response is found to be very stable with negligible change in steady state photocurrent, indicating the robustness of the $TiSe_2$ thin film as a photo-anode. Table 1 shows the comparison of present study with previously reported PEC-PD results, based on parameters such as applied bias, responsivity, detectivity, rise time and decay time.

Our work demonstrates PEC-PD with excellent responsivity, detectivity and quick switching. For 100 mV applied bias, the highest responsivity of 18.04 ± 0.45 μA/ W and detectivity of 7.36 ± 0.020 × 10^8 Jones are observed with rise time of 12 ms and decay time of 33 ms at the incident light power density of 8.47 mW/cm^2. At the same power density, performance of PEC-PD improved by application of higher bias voltages. The responsivity of (230.95 ± 2.14) μA/W and detectivity of (1.74 ± 0.02) x 10^9 Jones were achieved along with extraordinary rise time of 11 ms and a decay time of 50 ms at the applied bias of 500 mV, indicating strong potential of $TiSe_2$ for next generation low power optoelectronic device applications.

4. Conclusion

In present study, we have successfully fabricated and characterized high-performance and low-power PEC-PDs based on $TiSe_2$ thin films. DVT Grown $TiSe_2$ compound was confirmed to be nearly stoichiometric by FESEM-EDX. As grown powder was used to deposit $TiSe_2$ thin films via a controlled PVD technique, resulting in smooth thin film with excellent and uniformity as confirmed by AFM. XRD revealed hexagonal lattice structure of grown thin film whereas E_g and A_{1g} vibrational modes are captured by Raman spectroscopic investigation. These $TiSe_2$ thin films were utilized as working electrodes for PEC-PDs and performance evaluation of these devices revealed superior photodetection capabilities. Under a low applied bias of 100 mV, the device exhibited a responsivity of (18.04 ± 0.45) μA/W and a detectivity of (7.36 ± 0.020) x 10^8 Jones. With an increased bias of 500 mV, the responsivity and detectivity increased to (230.95 ± 2.14) μA/W and (1.74 ± 0.02) x 10^9 Jones respectively. Fast switching behaviour was observed with an average rise time of 12 ms and decay time of 33 ms. These impressive response time alongside low power operation suggests $TiSe_2$ thin film as a promising photoanode in PEC-PDs applications. Furthermore, the scalable fabrication process used in this study, coupled with the intrinsic advantages of $TiSe_2$ provides a viable pathway for refining photoelectrochemical photodetector technology. These results open up new way for the development of practical, next-generation optoelectronic devices utilizing $TiSe_2$-based architectures.

CRediT authorship contribution statement

Kevin Kantilal Bhanderi: Writing – original draft, Visualization, Methodology, Investigation, Formal analysis, Conceptualization. **Preet Deepankumar Vyas:** Writing – review & editing, Visualization, Investigation. **Jay Bhadreshbhai Ka. Patel:** Writing – review & editing, Visualization, Conceptualization. **Devang Dhorada:** Writing – review &

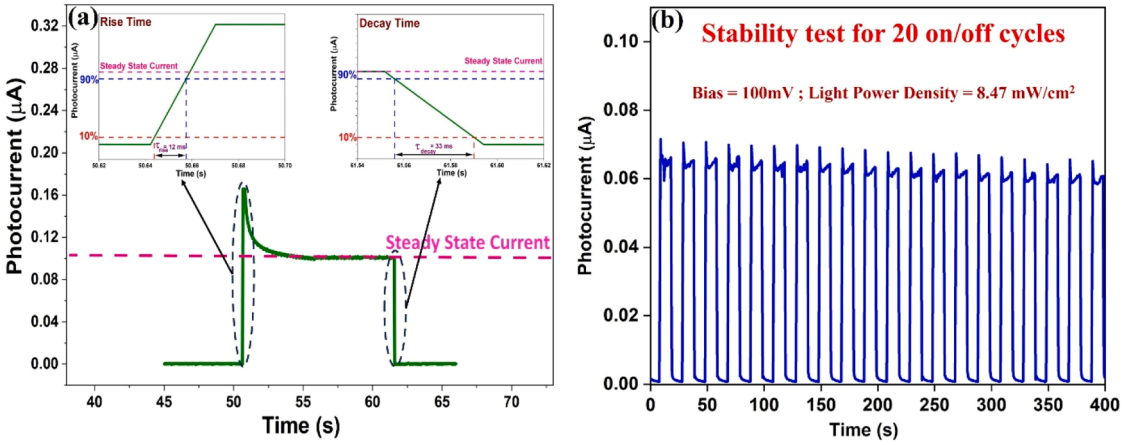

Fig. 6. Stability of $TiSe_2$ PEC-PD: (a) Rise time and Decay time at 100 mV bias to light Power density under 8.47 mW/cm^2 and (b) Stability test for 20 on/off cycles.

Table 1
Comparison of PEC-PD parameters with previously reported results.

Sr. No.	Materials	Responsivity (μA/W)	Electrolyte	Rise Time (ms)	Decay Time (ms)	Bias (V)	References
1.	$SnSe_2$ nanosheets	1.35	0.5 M Na_2SO_4	400	800	0	[68]
2.	GeSe Nanosheets	43.6 –73.6	0.1 M KOH	200	200	0.3	[69]
3.	$MnPS_3$	25.19	0.3 M Na_2SO_4	400	2100	0	[62]
4.	InSe nanosheets	3.3	0.2 M KOH	7000	7000	1	[70]
5.	SnS nanosheets	59.8	0.1 M Na_2SO_4	300	300	0.6	[71]
6.	SnS	18.2	0.5 M Na_2SO_4	600	300	0.4	[72]
7.	SnSe	41.4	0.5 M Na_2SO_4	1500	2000	0	[73]
8.	Nb_2C MXene	3.74	1 M KOH	150	100	0	[74]
9.	Bi_2Se_3 TF	17.5	0.5 M Na_2SO_4	-	-	0.6	[75]
10.	$TiSe_2$ TF	18.04	0.5 M Na_2SO_4	12	33	0.1	**This work**
11.	$TiSe_2$ TF	230.95	0.5 M Na_2SO_4	11	50	0.5	**This work**

editing, Investigation. **Akshaybhai J. Patel:** Writing – review & editing, Formal analysis. **Vismay Trivedi:** Writing – review & editing, Methodology. **Shubham Umeshkumar Gupta:** Writing – review & editing, Investigation. **Franco Mayanglambam:** Writing – review & editing, Resources. **Arun Anand:** Writing – review & editing, Resources. **Kireetkumar D. Patel:** Writing – review & editing, Visualization, Validation, Resources, Investigation, Conceptualization.

Declaration of competing interest

The authors confirm that they have no financial or personal conflicts of interest that could have influenced the outcome, interpretation, or reporting of the research detailed in this manuscript.

Acknowledgements

The authors K. K. B. and K. D. P. would like to acknowledge the Department of Physics, SPU, and USIC, SPU, for providing the necessary experimental facilities. Additionally, they also express their gratitude to the Shodh Fellowship (Shodh ref. ID. 2022016454) KCG, Government of Gujarat for funding this research. Authors thank IIT Guwahati INUP_i2i (5(1)/2021-NANO) and MeitY, Government of India, for their continuous support throughout the research. Special thanks are extended to Prof. S. H. Chaki and Dr. J. R. Gandhi for their help in performing the XRD measurements.

Supplementary materials

Supplementary material associated with this article can be found, in the online version, at doi:10.1016/j.electacta.2025.148035.

Data availability

Data will be made available on request.

References

[1] M. Kaur, P. Kumar, H.S. Ghotra, A review on advances in photoelectrochemical (PEC-type) photodetectors: a trending thrust research area, Int. J. Hydrog. Energy 49 (2024) 1095–1112, https://doi.org/10.1016/j.ijhydene.2023.11.018. Preprint at.
[2] Y. Yao, et al., Two-dimensional CuSe nanosheet array for high-performance photoelectrochemical photodetector using simulated seawater as electrolyte, Mater. Sci. Semicond. Process. 178 (2024).
[3] D. Yu, et al., Broadband and sensitive two-dimensional halide perovskite photodetector for full-spectrum underwater optical communication, Nano Res. 14 (2021) 1210–1217.
[4] H. Qiao, et al., Self-powered photodetectors based on 2D materials, Adv. Opt. Mater. 8 (2020), https://doi.org/10.1002/adom.201900765. Preprint at.
[5] A. Rymzhina, P. Sharma, V. Pavelyev, P. Mishra, N. Tripathi, Recent trends in the fabrication of photodetectors: a detailed analysis on the photodetection properties of new 2D-TMCs, Mater. Today Commun. 35 (2023), https://doi.org/10.1016/j.mtcomm.2023.106247. Preprint at.
[6] A. Pathak, et al., Advancing photodetection capabilities via Pb-induced modifications in SnSe crystals, J. Mater. Sci.: Mater. Electron. 35 (2024).
[7] A.N. Eroglu, C.T. Altaf, N.D. Sankir, M. Sankir, Design and production of mesh patterned photoelectrode with maskless laser lithography and device performance of perovskite derived/ZnO NRAs based photodetector, J. Mater. Sci.: Mater. Electron. 35 (2024).
[8] H. Chen, et al., High-responsivity natural-electrolyte undersea photoelectrochemical photodetector with self-powered Cu@GaN Nanowires network, Adv. Funct. Mater. 33 (2023).
[9] K. Ding, et al., Balancing carrier dynamics in oxygen-vacancy-tuned amorphous Ga2O3 thin-film self-powered photoelectrochemical-type solar-blind photodetector arrays for underwater imaging, Adv. Sci. (2024), https://doi.org/10.1002/advs.202407822, 10.1002/advs.202407822.
[10] Y. Luo, et al., Demonstration of photoelectrochemical-type photodetectors using seawater as electrolyte for portable and wireless optical communication, Adv. Opt. Mater. 10 (2022).
[11] Q. Gao, et al., Boosting photoresponse of self-powered photoelectrochemical photodetectors via Planar Interdigital Electrodes, Adv. Opt. Mater. 12 (2024).
[12] S. Zhang, et al., In2Se3 nanoparticles for use in self-powered photoelectrochemical photodetectors, Mater. Lett. 366 (2024).
[13] J. Xue, et al., Achieving a high-responsivity and fast-response-speed solar-blind photodetector for underwater optical communication via AlGaN/AlN/GaN heterojunction nanowires, ACS. Appl. Electron. Mater. 6 (2024) 4643–4652.
[14] J. Chen, et al., Performance limits and advancements in single 2D transition metal dichalcogenide transistor, Nano-Micro Lett. 16 (2024), https://doi.org/10.1007/s40820-024-01461-x. Preprint at.
[15] P.J. Wyndaele, et al., 2D TMDC aging: a case study of monolayer WS2 and mitigation strategies, Nanotechnology. 35 (2024).
[16] A. Rani, A. Verma, B.C. Yadav, Advancements in transition metal dichalcogenides (TMDCs) for self-powered photodetectors: challenges, properties, and functionalization strategies, Mater. Adv. 5 (2024) 3535–3562, https://doi.org/10.1039/d3ma01152f. Preprint at.
[17] H. Luo, et al., Differences in chemical doping matter: superconductivity in Ti1-xTaxSe2 but not in Ti1-xNbxSe2, Chem. Mater. 28 (2016) 1927–1935.
[18] *UNIVERSITY OF CALIFORNIA RIVERSIDE optoelectronics investigations of electron dynamics in 2D-TMD semiconductor heterostructure photocells: from electron-hole pair multiplication to phonon assisted anti-stokes absorption.* (2018).
[19] A.P. Singh, et al., Unravelling chemical etchant influences during assisted wet-transfer to obtain high quality MoS2 atomic layers, Appl. Surf. Sci. 669 (2024).
[20] M. Telkhozhayeva, et al., 2D TiS2 flakes for tetracycline hydrochloride photodegradation under solar light, Appl. Catal. B 318 (2022).
[21] M.S. Zafar, et al., Precise and prompt analyte detection via ordered orientation of receptor in WSe2-based field effect transistor, Nanomaterials 12 (2022).
[22] S. Nisar, et al., Gate-assisted MoSe2 transistor to detect the streptavidin via supporter molecule engineering, Mater. Today Nano. 24 (2023).
[23] Z. Xu, et al., Ultrafast charge transfer 2D MoS2/organic heterojunction for sensitive photodetector, Adv. Sci. 10 (2023).

[24] D. Kim, et al., The enhanced low resistance contacts and boosted mobility in two-dimensional p-type WSe2 transistors through Ar+ ion-beam generated surface defects, AIP. Adv. 6 (2016).
[25] A. Sengupta, A. Chanana, S. Mahapatra, Phonon scattering limited performance of monolayer MoS2 and WSe2 n-MOSFET, AIP. Adv. 5 (2015).
[26] X. Liu, et al., High performance WSe2 p-MOSFET with intrinsic n-channel based on back-to-back p-n junctions, Appl. Phys. Lett. 118 (2021).
[27] X. Yin, A. Teng, Z. Zeng, H. Meng, W. Wu, Facile and scalable preparation of 2D-MoS2/graphene oxide composite for supercapacitor, Ion. (Kiel) 28 (2022) 5223–5232.
[28] Z. Zheng, et al., Flexible, transparent and ultra-broadband photodetector based on large-area WSe2 film for wearable devices, Nanotechnology. 27 (2016).
[29] P. Vashishtha, et al., CVD-Grown Monolayer MoS2 and GaN Thin Film Heterostructure for a Self-Powered and Bidirectional Photodetector with an Extended Active Spectrum, ACS Appl. Mater. Interfaces 16 (2024) 31294–31303.
[30] D.H. Shin, W.U. Jeong, S.H. Choi, Strong dual-functional enhancement in flexible photodetection and photovoltaics of two-dimensional large-area WS2/MoS2Heterolayers by using a h-BN interlayer, ACS. Appl. Mater. Interfaces. 17 (2025) 48474–48482.
[31] H. Beydaghi, et al., Functionalized metallic transition metal dichalcogenide (TaS2) for nanocomposite membranes in direct methanol fuel cells, J Mater Chem Mater 9 (2021) 6368–6381.
[32] E. Navarro-Moratalla, et al., Enhanced superconductivity in atomically thin TaS 2, Nat. Commun. 7 (2016).
[33] P. Chauhan, et al., Flexible self-powered electrochemical photodetector functionalized by multilayered tantalum diselenide nanocrystals, Adv. Opt. Mater. 9 (2021).
[34] S. Karimi Khorrami, M. Berahman, M. Sadeghi, The electrical and transport properties of decorated ZrSe2 monolayer nano-sheet with copper clusters, Appl Phys Mater Sci Process 128 (2022).
[35] M. Salavati, Electronic and mechanical responses of two-dimensional HfS 2, HfSe 2, ZrS 2, and ZrSe 2 from first-principles, Front. Struct. Civ. Eng. 13 (2019) 486–494.
[36] L.M. Zhang, et al., Two-dimensional ZrSe2/ZrS2 heterobilayer tuned by electric field for optoelectronic devices, J. Korean Phys. Soc. 80 (2022) 606–612.
[37] P. Chen, L. Zhang, R. Wang, J. Shang, S. Zhang, Electronic and optical properties of the ZrS2/HfSe2 van der Waals heterobilayer with native type-II band alignment, Chem. Phys. Lett. 734 (2019).
[38] U.P. Sahoo, A. Mukherjee, P.K. Sahoo, Short-range charge density wave and bandgap modulation by Au-implanted defects in TiSe2, ACS. Appl. Electron. Mater. 4 (2022) 3428–3434.
[39] T.S. Walmsley, Y.Q. Xu, Enhanced photocurrent response speed in charge-density-wave phase of TiSe2-metal junctions, Nanoscale 13 (2021) 11836–11843.
[40] A. Nomura, S. Demura, S. Ohta, S. Kobayashi, H. Sakata, Emergence of a thermal hysteresis of electrical resistance by thinning in 1T-TiSe2, J Low Temp Phys 213 (2023) 215–222.
[41] A. Saini, N.K. Karn, K. Kumar, R.P. Aloysius, V.P.S. Awana, Drastic suppression of CDW (Charge Density Wave) by Pd addition in TiSe2, J. Supercond. Nov. Magn. 36 (2023) 3–9.
[42] L. Chen, et al., TiSe2-mediated sonodynamic and checkpoint blockade combined immunotherapy in hypoxic pancreatic cancer, J. Nanobiotechnology. 20 (2022).
[43] C. Xiong, et al., Nano t-Se peninsulas embedded in natively oxidized 2D TiSe2 enable uniform and fast memristive switching, ACS. Appl. Mater. Interfaces. 15 (2023) 23371–23379.
[44] H. Wang, et al., Large-area atomic layers of the charge-density-wave conductor TiSe2, Adv. Mater. 30 (2018).
[45] B. Yan, et al., Broadband 1T-titanium selenide-based saturable absorbers for solid-state bulk lasers, Nanoscale 10 (2018) 20171–20177.
[46] U. Paliwal, P. Tanwar, K.B. Joshi, Structural, electronic and thermoelectric properties of monolayer TiSe2, J. Mol. Model. 30 (2024).
[47] J. Yang, et al., S-doped TiSe2 nanoplates/Fe3O4 nanoparticles heterostructure, Small. 13 (2017).
[48] *SAFETY DATA SHEET according to regulation (EC)*. (1907).
[49] K. Kadiwala, E. Dipans, L. Dipane, E. Butanovs, B. Polyakov, Towards scalable synthesis of TiSe2 and VSe2 thin films, Latv. J. Phys. Tech. Sci. 61 (2024) 13–22.
[50] S.S. Jaswal, Lattice dynamics of TiSe2, Phys. Rev. B 20 (1979).
[51] W. Xia, et al., Pressure-induced re-entrant superconductivity in transition metal dichalcogenide TiSe2, Small 20 (2024) 2402749.
[52] Z.L. Wang, G. Chen, X. Zhang, D. Tang, The first-principles and BTE investigation of phonon transport in 1T-TiSe2, Phys. Chem. Chem. Phys. 23 (2021) 1627–1638.
[53] C. Metzger, et al., Biaxial strain in graphene adhered to shallow depressions, Nano Lett. 10 (2010) 6–10.
[54] C.I. Medel-Ruiz, R. Chiu, J.R. Sevilla-Escoboza, F.J. Casillas-Rodríguez, Nanoscale surface roughness effects on photoluminescence and resonant raman scattering of cadmium telluride, Appl. Sci. (Switz.) 14 (2024).
[55] P.D. Vyas, et al., Seawater-powered PEC photodetectors based on a layered metal dichalcogenide for marine underwater optical communication, ACS Sustain. Chem. Eng. 13 (2025) 12010–12021.
[56] M. Khademi, D.P.J. Barz, Structure of the electrical double layer revisited: electrode capacitance in aqueous solutions, Langmuir. 36 (2020) 4250–4260.
[57] K. Doblhoff-Dier, M.T.M. Koper, Modeling the Gouy-Chapman diffuse capacitance with attractive ion-surface interaction, J. Phys. Chem. C 125 (2021) 16664–16673.
[58] C. Duan, et al., FePS3Nanosheet-based photoelectrochemical-type photodetector with superior flexibility, J. Phys. Chem. C 125 (2021) 9526–9533.
[59] S.U. Gupta, et al., Cryotronic low-powered strained polymorphic photodetector functionalized by Palladium Incorporated tin diselenide, Adv. Opt. Mater. 10 (2022).
[60] M.T. Mayer, C. Du, D. Wang, Hematite/Si nanowire dual-absorber system for photoelectrochemical water splitting at low applied potentials, J. Am. Chem. Soc. 134 (2012) 12406–12409.
[61] P. Vashishtha, A. Dash, S. Walia, G. Gupta, Self-bias Mo–Sb–Ga multilayer photodetector encompassing ultra-broad spectral response from UV–C to IR–B, Opt. Laser. Technol. 181 (2025).
[62] X. Geng, et al., Electrolyte-controlled photoelectrochemical photocurrent switching effect in high-performance self-powered broadband photoelectrochemical-type photodetectors based on MnPS3 nanosheets, ACS. Appl. Mater. Interfaces. 15 (2023) 55938–55947.
[63] H. Zhang, H. Wang, J. Xuan, Rational design of photoelectrochemical cells towards bias-free water splitting: thermodynamic and kinetic insights, J. Power. Sources. 462 (2020).
[64] P. Vashishtha, et al., Multiband spectral response inspired by ultra-high responsive thermally stable and self-powered Sb2Se3/GaN heterojunction based photodetector, Surf. Interfaces 42 (2023).
[65] M. Zhang, et al., Ultrathin In2O3 nanosheets toward high responsivity and rejection ratio visible-blind UV photodetection, Small 19 (2023).
[66] S.U. Gupta, et al., Optical switching device based on a crystalline SnSe2Photodetector in diverse conditions, ACS Appl. Electron Mater. 3 (2021) 4859–4869.
[67] M. Mokhtarimehr, S.A. Tatarkova, Photocurrent transients of thin-film solar cells, J. Opt. Soc. Am. B 34 (2017) 1705.
[68] M. Patel, S. Bhakhar, G.K. Solanki, Showcasing a self-powered photoelectrochemical photodetector with ultrasonically exfoliated SnSe2 nanosheets, J. Mater. Sci.: Mater. Electron. 35 (2024).
[69] D. Ma, et al., Ultrathin GeSe nanosheets: from systematic synthesis to studies of carrier dynamics and applications for a high-performance UV-vis photodetector, ACS Appl. Mater. Interfaces 11 (2019) 4278–4287.
[70] Z. Li, et al., High-performance photo-electrochemical photodetector based on liquid-exfoliated few-layered InSe nanosheets with enhanced stabilit, Adv. Funct. Mater. 28 (2018).
[71] W. Huang, et al., Black-phosphorus-analogue tin monosulfide: an emerging optoelectronic two-dimensional material for high-performance photodetection with improved stability under ambient/harsh conditions, J. Mater. Chem. C. Mater. 6 (2018) 9582–9593.
[72] X. Xu, et al., High performance UV–Vis photodetectors based on tin monosulfide film synthesized by physical vapor deposition, Appl. Surf. Sci. 597 (2022).
[73] C. Lu, et al., Direct Z-scheme SnSe2/SnSe heterostructure passivated by Al2O3 for highly stable and sensitive photoelectrochemical photodetectors, ACS. Appl. Mater. Interfaces 15 (2023) 6156–6168.
[74] L. Gao, et al., Applications of few-layer Nb2C MXene: narrow-band photodetectors and femtosecond mode-locked Fiber lasers, ACS. Nano 15 (2021) 954–965.
[75] Y. Ye, R. Yu, Z. Huang, H. Qiao, X. Qi, Photoelectrochemical photodetector based on electrodeposited Bi2Se3 film with superior performance, Appl. Phys. A Mater. Sci. Process 130 (2024).